Fuel 288 (2021) 119451

Contents lists available at ScienceDirect

Fuel

journal homepage: www.elsevier.com/locate/fuel

Full Length Article

Simulating combustion of a seven-component surrogate for a gasoline/ethanol blend including soot formation and comparison with experiments

Alberto Cuoci [a], C. Thomas Avedisian [b,*], Jordan D. Brunson [b], Songtao Guo [b], Alireza Dalili [b], Yujie Wang [b], Marco Mehl [a,c], Alessio Frassoldati [a], Kalyanasundaram Seshadri [d], John E. Dec [e], Dario Lopez-Pintor [e]

[a] CRECK Modeling Lab, Department of Chemistry, Materials, and Chemical Engineering, Politecnico di Milano, Piazza Leonardo da Vinci 32, 20133 Milano, Italy
[b] Sibley School of Mechanical and Aerospace Engineering, Cornell University, Ithaca, NY 14853, USA
[c] Physical and Life Sciences, Lawrence Livermore National Laboratory, Livermore CA 94551, USA
[d] Department of Mechanical and Aerospace Engineering, University of California, San Diego, CA 92093, USA
[e] Combustion Research Facility, Sandia National Laboratories, Livermore, CA 94551, USA

ARTICLE INFO

Keywords:
Ethanol
Gasoline
Numerical analysis
Droplets
Surrogates
Soot formation
Combustion

ABSTRACT

Combustion of a seven-component surrogate for a research grade 87 octane gasoline mixed with 10% ethanol is investigated experimentally and numerically from the perspective of an isolated droplet burning under conditions that promote one-dimensional gas transport. The numerical analysis included a kinetic mechanism comprised of 398 species and 24,814 reactions and a soot model that accounted for nucleation, surface growth, coalescence/aggregation of soot particles, and luminous flame radiation. Measurements of droplet and flame diameters were made for an initial droplet diameter (D_o) of approximately 0.63 mm. The simulations agreed well with the measurements including the location of the soot shell. Preferential vaporization was revealed by simulations of the liquid concentrations in the droplet. Predicted peak soot volume fractions coincided with temperatures between 1300 K and 1400 K as a soot inception temperature. Simulations were also carried out for D_o between 0.25 mm and 5 mm to explore the effect of radiation and D_o on burning. Below 0.25 mm radiation was negligible and burning rates and flame temperatures converged to a single value. Increasing D_o up to 1.8 mm lowered the burning rate with luminous radiation having a strong effect. When radiation was entirely removed from the model the burning rate was nearly constant. Above $D_o = 2$ mm droplets extinguished almost immediately after ignition. The flame temperature decreased with increasing D_o while it increased when radiation was omitted. The simulations show that soot precursors including polyaromatic hydrocarbons were concentrated around the soot shell.

1. Introduction

Dwindling supplies of crude oil have motivated strategies to offset the depletion of petroleum-based fuels. Blending transportation fuels (gasoline, diesel, jet) with biofuels is a well-known option. The most widely used biofuel additive to gasoline for light-duty vehicles is ethanol at 10% by volume ('E10'), though many others are being considered [1,2]. E10 is a benchmark gasoline/biofuel system which provides a point of comparison with alternatives. For example, ethanol as an additive has been compared to alternatives such as iso-butanol [3] and to fuel blends that tailor autoignition reactivity with fuel equivalence ratio [4]. E10 has also been used as a fuel to benchmark the potential for partial fuel stratification in low temperature gasoline combustion engines [5].

Prior work on E10 combustion involved engine testing which provided useful information about system-level and end-use performance [5–7]. From the standpoint of detailed modeling, it is necessary to have accurate information on the inputs to detailed simulations, such as a fuel's combustion kinetic mechanism and property database. An engine is too complex of a system to validate a kinetic mechanism or thermal and transport property database, or as a means to evaluate models for forming particulate matter (i.e., soot) because of the complex flow dynamics (turbulence, and swirl) of the in-cylinder environment. A combustion configuration with a simplified transport is a useful alternative to address these challenges.

* Corresponding author.
E-mail address: cta2@cornell.edu (C.T. Avedisian).

https://doi.org/10.1016/j.fuel.2020.119451
Received 16 July 2020; Received in revised form 30 September 2020; Accepted 6 October 2020
Available online 24 December 2020

Nomenclature

a	major-axis
b	minor-axis
$c_{p,g}$	mean gas heat capacity
$c_{p,g,i}$	heat capacity of gas species i
$c_{p,L}$	mean liquid heat capacity
D	droplet diameter
D_f	flame diameter
D_o	initial droplet diameter
D_s	soot shell diameter
FSR	D_f/D
f_v	soot volume fraction
$H_{g,i}$	enthalpy of gas species i
$h_{fg,i}$	heat of vaporization of species i
K	droplet burning rate
k_g	mixture gas thermal conductivity
k_L	mixture liquid thermal conductivity
$J_{L,i}$	molar diffusion flux of species i (liquid phase)
$j_{L,i}$	mass diffusion flux of species i (liquid phase)
N_g	number of components in the gas phase
N_L	number of components in the liquid phase
p_i	partial pressure of species i (gas phase)
p_i^v	vapor pressure of species i
q_R	radiative heat transfer flux
Q_c	heat conduction from the flame to the droplet
Q_R	radiant heat loss
r	radial coordinate
R_d	droplet radius
Ra_D	$=g\beta\,(T_f\text{-}T_\infty)D^3/(\alpha\,\nu)$
Re_D	$=v_{rel}\,D/\,\nu$
R_∞	computational domain radius
SSR	D_s/D
T	temperature
T_b	fuel boiling point
T_L	liquid temperature
T_c	critical temperature
T_g	gas temperature
T_f	flame temperature
t	time
v_{rel}	relative velocity between the droplet and surrounding
v_g	radial gas velocity
$V_{g,i}$	gas diffusion velocity of species i in gas
W_{tot}	mass flow rate
$X_{L,i}$	mole fraction of liquid species i
$Y_{g,i}$	mass fraction of gas species i
$Y_{L,i}$	mass fraction of liquid species i

Greek

α	gas thermal diffusivity
α_g^k	absorption coefficient of species k in gas
β	gas thermal expansion coefficient
ϕ_i	fugacity coefficient of species i in gas phase
Γ_{ij}	activity matrix coefficients (liquid phase)
γ_i	activity coefficient of species i in liquid phase
Λ_{ij}	Stefan-Maxwell binary diffusion coefficients (liquid phase)
ρ_g	mean gas density
$\rho_{g,i}$	density of gas species i
ρ_L	mean liquid density
ν	gas kinematic viscosity
$\omega_{g,i}$	formation rate of gas species i

The study of E10 combustion reported here is framed around the subgrid element of a spray – an isolated droplet – as a platform for examining the complications noted above. In particular, an isolated droplet of E10 is considered burning under conditions where a one-dimensional (1-D) gas transport is promoted. A distinctive feature of the 1-D transport configuration for droplet burning of soot-producing fuels is the confinement of soot aggregates into a shell-like structure which aids tracking soot and predicting the soot concentration field. Moreover, the simplicity of the 1-D configuration enables convolving liquid and gas phase transport which is important in practical liquid fuel burning systems.

E10 is a multicomponent collection of many organic liquids that often exhibits a seasonable variability. This problem has been addressed by developing a calibration fuel termed 'RD5-87-2A' for E10 which is also highly multicomponent but not subject to compositional variations in refining. However, RD5-87-2A is still too complex to enable simulating its combustion. A 'surrogate' for RD5-87-2A was recently developed with potential to mimic its performance and enable simulations because of its reduced compositional complexity. This study addresses the efficacy of the RD5-87-2A surrogate to mimic performance of RD5-87-2A by detailed numerical simulations of the 1-D droplet configuration.

The RD5-87-2A surrogate is a seven-component mixture (termed 'S3′) comprised of (volume fraction) n-heptane (0.11), n-pentane (0.088), iso-octane (0.405), cyclo-pentane (0.055), toluene (0.18), 1-hexene (0.063) and ethanol (0.099) [7]. The present study uses this mixture to access the droplet combustion physics of RD5-87-2A and thereby E10 through detailed numerical modeling that can serve as the basis for validating a detailed kinetic mechanism for the numerical model. The results are compared with the experimental database reported in this paper.

While some aspects of the droplet burning considered in the present study have been incorporated into various numerical models, the totality of what is included in the present study has not been combined into a single treatment of droplet burning. In particular, the following elements have not previously been combined into a single comprehensive numerical analysis of droplet burning and so is a new contribution: a surrogate fuel comprised of seven miscible components; a detailed combustion kinetic oxidation mechanism with a large number of reactions that incorporates soot chemistry; radiation for non-luminous and luminous emissions; the effects of water condensation on burning (due to the presence of ethanol); thermal and transport properties that depend on temperature and concentration; unsteady gas and liquid transport, tracking the moving boundary of the burning droplet; formation of soot and creation of the soot shell. Experimental results from the present study provide a form of validation for these effects in the numerical model described.

Recent detailed numerical modeling of droplet combustion with a multistep kinetic mechanism considered single component and binary mixtures without incorporating a soot model [8–14]. Three previous studies are known to have included soot formation all for a single component fuel. In two of these [15,16] only a one-step oxidation reaction was considered so that soot precursors could not be predicted. A third study [17] incorporated a detailed kinetic mechanism with a more sophisticated soot model based on the discrete sectional method. Prediction of the soot shell was based on matching thermophoretic and Stefan velocities.

The importance of thermal and transport properties in the numerical model is addressed using temperature and concentration-dependent correlations because of their importance in combustion modeling [18]. Ethanol is miscible in water in all proportions so the potential for water vapor generated at the droplet flame and diffusing to the droplet

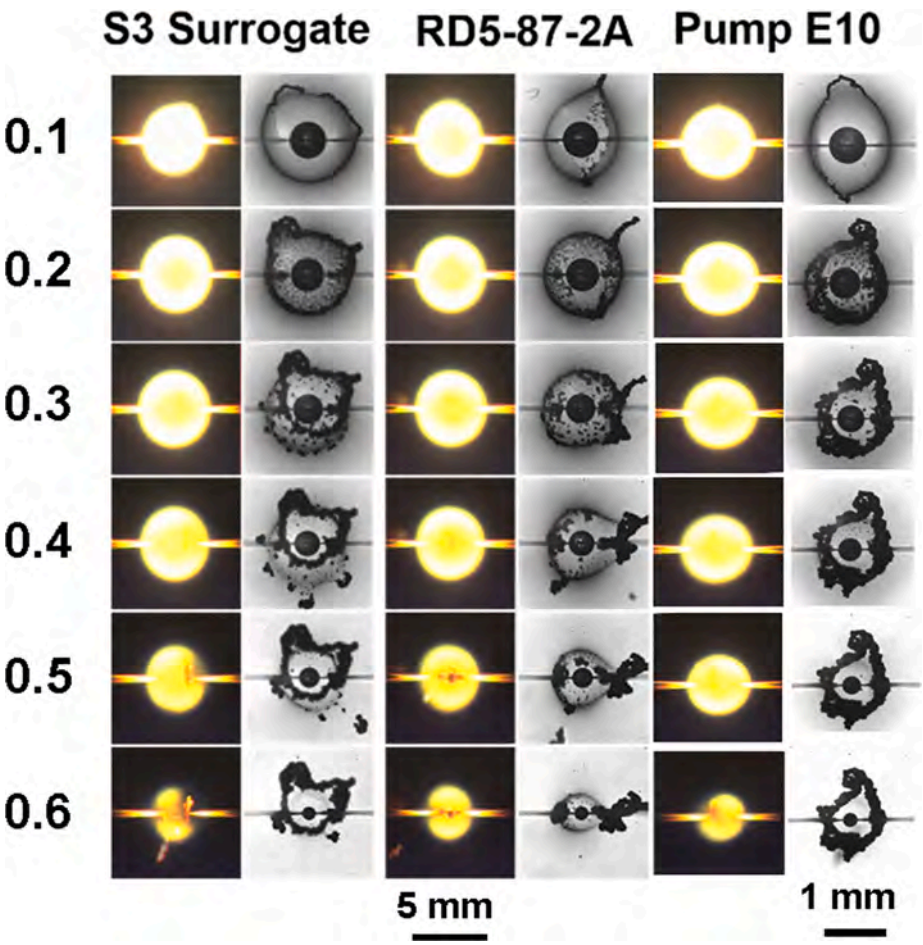

Fig. 1. Representative photographs from experiments for S3, RD5-87-2A and a pumpE10 (87 octane). The column of numbers are the elapsed times in seconds after ignition. Initial diameters were as follows: for S3, $D_o = 0.64$ mm; for RD5-87-2A, $D_o = 0.62$ mm; for pumpE10, $D_o = 0.64$ mm. Yellow circles are due to soot incandescence. Bright horizontal lines arise from intersection of the flame with the SiC fiber supports. Soot shells are visible. The 5 mm scale at the bottom refers to the flame (color) images and the 1 mm scale refers to the black and white images. (For interpretation of the references to color in this figure legend, the reader is referred to the web version of this article.)

where it can condense on the droplet surface is included in the model. This effect was first considered for ethanol droplet combustion [19] and is a general consideration for any alcohol additive to gasoline. For alcohols with lower solubility in water (e.g., iso-butanol) the effect may be less important.

The initial droplet diameters (D_o) examined experimentally in this study were in the range of 0.62 mm to 0.64 mm. Droplets in spray flames are typically much smaller by an order of magnitude. Moreover, significant droplet/droplet interactions are present in the 3-D transport field within combustion engines. Therefore, the relevance of isolated droplet studies in the context of in-cylinder processes of combustion engines should be considered.

The relevance of isolated droplet combustion, especially when the thermal and fluid transport process is reduced to 1-D as in the present study, is to bring into the kinetic mechanism validation process the liquid phase, specifically to assess the ability of heat release by fuel oxidation at the flame to evaporate the fuel at rates consistent with the experimental measurements. This process is important in practical systems. Moreover, it is known that fuel oxidation chemistries are closely tied to droplet evaporation and flame processes [20]. Incorporating this connection is not possible when the liquid phase is eliminated by pre-vaporizating it to produce a purely gas-phase combustion process resulting in a kinetic mechanism that is untested for evaporating the liquid fuel.

From a modeling perspective pre-vaporizing the liquid and creating conditions that promote a 0-D or 1-D gas transport as in shock tubes, jet stirred reactors, homogeneous reactors and other configurations facilitates detailed numerical simulations with a number of commercially available and rigorous codes. The 1-D droplet flame configuration has not until recently enjoyed a similar level of numerical rigor. A detailed model of the 1-D droplet burning case is well positioned to validate a kinetic mechanism in the context of combustion of a liquid fuel. The present study is motivated by that potential.

This paper extends capabilities to simulate multicomponent fuels to include soot formation and luminous and non-luminous radiation (along with variable properties and unsteady gas and liquid transport that have been considered in past work) that provide a more robust computational tool for analysis. The comparisons shown here suggest that the 1-D droplet flame configuration is potentially useful for informing the oxidation chemistry of complex fuel mixtures to enable more robust mechanisms that better create thermal conditions for fuel evaporation and ignition in more complex configurations.

The next sections describe the experimental methodology for creating near-spherically symmetric burning conditions followed by a discussion of the experimental and numerical results to predict its burning.

2. Experimental design and data analysis

The experiments were designed to provide a burning environment that promoted a 1-D transport configuration. This was achieved by eliminating convective effects arising from buoyancy and forced flow. This situation is achieved by conditions characterized by appropriately defined Reynolds and Rayleigh numbers being small, $Re_D \ll 1$ and $Ra_D \ll 1$ respectively. The variable used to make $Ra_D \ll 1$ was gravity, specifically by carrying out the experiments under low gravity

Table 1
Selected properties of the S3 surrogate components [24].

Species	formula	MW (kg/kmol)	T_b (K)	T_c (K)	ρ_L (kg/m^3)	h_{fg} (kJ/kg)	volume fraction	mole fraction
n-heptane	C_7H_{16}	100.21	372	540	684	316	0.1112	0.09
n-pentane	C_5H_{12}	72.15	309	470	626	358	0.0875	0.09
iso-octane	C_8H_{18}	114.23	372	544	692	271	0.4049	0.29
cyclo-pentane	C_5H_{10}	70.14	322	512	745	389	0.0551	0.07
toluene	C_7H_8	92.14	384	592	867	384	0.1794	0.20
1-hexene	C_6H_{12}	84.16	337	504	673	372	0.0633	0.06
ethanol	C_2H_6O	46.07	352	516	789	839	0.0986	0.20

conditions (ranging between 10^{-4} and 10^{-2} of earth's normal gravity). Re_D was made small by performing the experiments in quiescent air and by physically restricting droplet motion by deploying them at the intersection of two 14 μm SiC fibers. After each experimental run, the fibers were replaced by new fibers to guarantee that there was no residual soot left from a previous experimental run. This design was developed to minimize the influence of the fiber supports on the burning process [21]. The experiments were carried out in a sealed chamber in free-fall. For the S3 droplet sizes examined burning times were under 0.7 s. The free-fall distance was 7.6 m which provided about 1.2 s of experimental time. Further details of the experimental design and procedures are given in [21–23].

Droplets were ignited by spark discharges from two pairs of electrodes positioned on opposite sides of the droplet. The spark discharge circuitry permitted accurate measurement of the spark 'on' time and duration. For the experiments reported here, the intersection of the fibers was centered between the two electrode pairs with a gap of approximately 2.0 mm between them. The electrode tips were positioned approximately 1.8 mm from the intersection. The electrical circuit to generate sparks had the capability to record and control the spark energy. The intent with ignition was to keep the ignition disturbance of the gas at the lowest level possible to just ignite the droplets. The minimum energies to achieve ignition of the fuel systems investigated (and the corresponding 'on' times of the sparks) were 71.2 mJ (261 μ s), 61.2 mJ (225 μ s), and 64.9 mJ (242 μ s), for pumpE10, RD5-87-2A, and S3, respectively. The different values were the result of differing fuel properties

After deploying a droplet onto the SiC fibers the instrumentation package was held in place by an electromagnet. Terminating power to the magnet then released the package into free-fall. Sparks were activated 150 ms into the fall to minimize separation-induced disturbances from the on-board components. After ignition, the two electrode pairs were rapidly retracted so that they would not influence burning.

An experiment was terminated by impact of the instrumentation package into a foam-filled cylindrical steel tank. The diagnostics on the package had to be stable and secured so as not to be disturbed by the impact. This consideration precluded using laser-based systems for monitoring the burning process. Digital video imaging was used exclusively to record the burning process. The video record constituted the 'raw' data of the experiments. The video records of burning were obtained using a Canadian Photonics MS-80K (3.9 megapixel; 200 fps) black-and-white (BW) camera which is well suited to show the droplet and soot structure. The flame shape and luminosity were recorded using a Hitachi HV-C20 camera (0.3 megapixel; 30 fps). These framing rates were sufficient to capture the physics of the burning process including the evolution of droplet, flame and soot shell diameters and phenomena such as flash boiling and flame extinction. Very fast transient processes such as flash boiling were a rare occurrence so that higher frame rate cameras were not needed.

Video images for the BW camera were illuminated from the back by a single wavelength LED (Prismatix Mic-LED with BLCC-04; 637 nm) light source. The color images were self-illuminated by soot incandescence. Fig. 1 shows representative images of burning histories of the three fuels

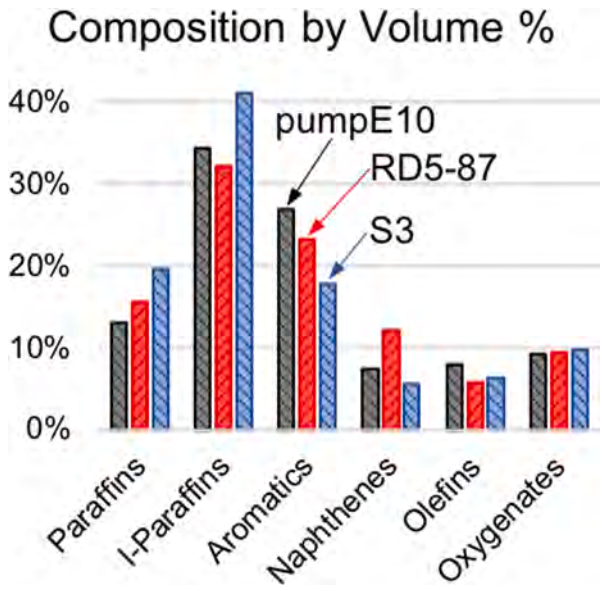

Fig. 2. Compositions (volume percent) of pumpE10, RD-587, and S3 grouped by chemical classes.

investigated (discussed in Section 5).

Central to the process of data acquisition is the ability to extract quantitative measurements from images like those shown in Fig. 1. Because of the high sooting propensity of the fuel systems investigated it was not always possible to analyze video images that showed a large amount of soot in the field of view using an automated data extraction process. Instead, a manual method was used in such cases with each video image needing to be processed individually. This effort was time-consuming and accomplished with the aid of imaging software (ImagePro Plus (Rockville, MD, USA) software). A virtual ellipse as a more general droplet shape was manually positioned around the droplet, flame or soot shell using the analysis software. A region of interest was selected and measurements of equivalent diameter made of the major ('a') and minor ('b') lengths of the ellipse based on cross-sectional area, $(a \times b)^{1/2}$. Operator skill is required to properly position the ellipse around the flame or soot shell (Fig. 1). Different operators were calibrated against each other for consistency.

Flame diameters were more difficult to measure accurately because the flame boundary was much less well defined than the droplet boundary. The flame diameter was measured using the line-of-sight diagnostic in the IMAGE PRO software on a 24 in. Dell 4 K ultra HD monitor. The monitor revealed each pixel of an image. A threshold value or maximum gradient for the flame boundary was not used. The flame boundary was user-determined and discerned by eye. Images were independently analyzed by different users to ensure consistency.

An important consideration for mixture droplets is to ensure that the droplet composition at the time of ignition is the same as the initially

prepared composition. Differences can arise from exposure of the mixture droplet to air due to preferential vaporization during set-up prior to conducting an experiment. The experimental procedure developed here limits such exposure to about 1 s or less prior to deployment and ignition of the droplet. Prior work [23] showed this time to be sufficient to maintain the initially prepared compositions of hydrocarbon mixtures for the procedures employed here. Additionally, chemical analysis was carried out to verify that the initial composition did not change from the initially prepared composition.

3. Fuel systems

3.1. Fuel chemical analysis

The fuels examined were RD5-87-2A, the S3 surrogate, and E10 purchased from a service station in Syracuse, NY (April 2019), termed 'pumpE10'. RD5-87-2A was provided by Sandia National Laboratories (SNL, California). The S3 surrogate was developed in a collaboration between Lawrence Livermore National Laboratory (LLNL) and SNL (Section 3.2) and prepared in-house on a volumetric basis using the compositions listed in Table 1.

The fuels were chemically analyzed to provide their composition and fractional amounts based on ASTM D6729. Results of the detailed hydrocarbon analysis (DHA) are shown in Fig. 2 which groups the compositions into six general hydrocarbon classes with the fractional amounts shown (volume fraction).

The three fuels are qualitatively similar. Oxygenates are the best matched chemical class because all three fuels contained ethanol at 9.86%. Chemical differences are explained by the different levels of complexity: S3 contains 7 distinct components while RD5-87-2A and pumpE10 contain several hundred components each.

3.2. S3 surrogate formulation

The S3 surrogate was formulated by matching both the composition of the real fuel and its ignition characteristics. The fuel composition was first determined and components grouped into basic hydrocarbon classes, similar to the methodology described in [25]. Fig. 2 shows results for the fuels examined. Representative components for each hydrocarbon class were then selected as further discussed below, with the added consideration that the surrogate components should be relatively abundant and have validated combustion kinetic mechanisms. Once the surrogate components were selected, their fractional amounts were determined.

One approach for determining the fractional amounts of a surrogate makes use of a regression algorithm that matches properties or 'targets' of the surrogate selected by the user with those of the fuel by minimizing an objective function. An example of this approach is described in [26]. Target values could be predicted if reliable methodologies exist to do so, otherwise they must be measured. The results depend on the choice of weighting functions of the target properties in the regression. Alternatively, surrogate component concentrations could be selected as the same values as the chemical classes of the DHA in which the components belong, then adjusted to improve performance of the surrogate in the combustion configuration of interest [27]. The approach taken here was a combination of these methods.

The surrogate components were selected to represent the six hydrocarbon classes and expanded to include components that account for variations of reactivity within key hydrocarbon classes. For instance, the $\leq$C5 n-alkanes are represented by n-pentane which is the most abundant n-alkane in E10, while C6 and larger n-alkanes are represented by n-heptane to account for the fact that the reactivity of the shorter and longer n-alkanes differ significantly. Several recent investi gations [25,28] have pointed out the importance of including different species within hydrocarbon classes to account for variations of autoignition reactivity with carbon number.

The above approach is limited by the palette of species available in the chemical kinetic model. For example, among all the cycloalkane species, only the chemistry of cyclopentane is included in the chemical kinetic mechanism. Therefore, the amount of cyclopentane in the surrogate was set to match the DHA value for this species, while the more reactive C6 and larger cycloalkanes are represented by including additional amounts of iso-octane and n-heptane. The relative amounts of these additional alkanes were adjusted to match the RON (research octane number) and MON (motor octane number) of the surrogate to that of the fuel following the methodology described in [26]. For this reason, the concentrations of n-alkanes and iso-alkanes in the surrogate are higher than those of the real fuel (as shown in Fig. 2).

RON and MON alone are insufficient to characterize the reactivity of a fuel at conditions different from those of the RON and MON tests. To solve this issue, the methodology used in this paper incorporates well-mixed ignition data obtained from homogeneous charge compression ignition (HCCI) engine experiments. Gas-phase simulations of a homogeneous reactor (HR) were performed using the LLNL detailed chemical-kinetic mechanism for a gasoline surrogate [29] to estimate the surrogate's autoignition reactivity at premixed engine-like conditions, and the results were compared to HCCI engine data. While a HR reactor is very different from the droplet flame configuration of interest here, simulations of a HR reactor may inform minor adjustments of surrogate compositions to improve agreement with autoignition data. The DHA fractional amounts, RON and MON, and autoignition reactivity at HCCI engine conditions were used as targets in an iterative process, in which adjustments to the surrogate composition were made until convergence was achieved. The components and their volume fractions that resulted from this effort are listed in Table 1.

There is no obvious reason why a surrogate developed using information from one combustion configuration would be applicable to another. That it may be applicable is an intriguing possibility. A crucial test here is a direct experimental comparison of the S3 surrogate with RD5-87-2A. Section 5 discusses results of such a comparison for the droplet configuration.

4. Detailed numerical model

4.1. Formulation and solution of the governing equations

Spherical symmetry is assumed to enable solving the mass, species, and energy differential equations. The governing differential equations and boundary conditions are listed in Appendix A. The equations were solved in a coupled approach using the OpenSMOKE++ framework [30]. The partial differential equations were transformed into a set of differential–algebraic equations (DAEs) and then solved using the finite difference method, applied on a non-uniform and moving mesh in spherical coordinates using the method of lines.

The DAE system is very 'stiff' because of the existence of a wide range of characteristic times associated with the chemical species and chemical reactions. Radicals such as OH, O and H have short characteristic times, on the order of $10^{-9}/10^{-8}$ s, while the formation of large soot particles requires much longer times, on the order of 10^{-3} s. The DAE system was solved in a fully-coupled way using an implicit solver based on the backward differentiation formula (BDF) method, specifically conceived for very stiff equations associated with chemical reactions.

Implicit solvers are the only viable approach to solving stiff DAE systems, but they are expensive in terms of computational time because of the need to evaluate and factorize the Jacobian matrix associated with the equations. In order to reduce the computational cost related to the Jacobian treatment, two approaches were considered: i) the Jacobian matrix elements were split into a convection + diffusion contribution and calculated numerically, and a chemical contribution associated with the reactions only was determined analytically; and ii) dummy variables/equations were introduced in the DAE system to force the Jacobian matrix to have a structured tri-diagonal-block sparse pattern. This

last point is very important from a computational point of view because we have the possibility to use special numerical algorithms to exploit this specific sparsity structure. Additional details about the numerical solution of a DAE system for the 1-D droplet configuration can be found in [9]. The simulations reported in the present paper were carried out on a single core Intel Xeon CPU X5675 computer with a 3.07 GHz processor. Typical computational times ranged between 24 and 36 h.

Most of the numerical issues in the solution were concentrated in the initialization of the solution. In order to proceed with the solution in time it is first necessary to solve the non-linear algebraic equations that describe, at $t = 0$, the thermodynamic equilibrium conditions at the droplet/gas interface. In some situations, the solution of these equations, carried out via a quasi-Newton method, does not converge to a proper solution. In such conditions it is necessary to provide a different first guess solution.

The numerical model makes no assumptions about the evaporation process or internal liquid phase transport beyond the methodology for computing the bubble point temperature of the mixture. Mass transport in the droplet and surrounding gas is by radial convection and diffusion. In particular, there is no provision for generating instabilities as, for example, by thermo capillary effects created by surface tension gradients that could lead to internal liquid motion and a non radial transport process. The existence of such instabilities would be contrary to the assumption of transport symmetry and so are excluded from consideration.

Ignition was numerically achieved by the imposition of a short (~100 ms) high temperature zone (2000 K to 2500 K) that transferred heat to the droplet, followed by a non-uniform temperature radial profile peaking at about 2200 K (according to the approach suggested in [11]). These ignition parameters were unable to numerically ignite droplets smaller than about 0.25 mm. Below this value evaporation occurred so quickly that droplets disappeared before they could be ignited. Only by changing the thermal parameters of ignition could smaller droplets be numerically ignited. Droplets in the range of 0.25 mm to about 1.8 mm were numerically ignited and burned to completion. For $D_o > 2.0$ mm the flame was so large that radiative extinction occurred almost immediately. Further discussions are given in Section 6.

The importance of fuel properties on the droplet burning process cannot be overstated. Special attention was devoted to the treatment of properties including diffusion in the liquid phase (based on the Stefan-Maxwell theory), the description of thermodynamic equilibrium at the gas/liquid interface (based on the UNIFAC approach), and to modeling soot formation. The Supplementary Material section (SM1) provides details concerning the estimation of thermodynamic and transport properties of the gaseous and liquid species. Based on previous experiences [31], gas thermal conductivity (k_g) was shown to play an important role in determining the vaporization rate of the droplet, which is not surprising given that the classical theory of droplet burning predicts that $K \propto (k_g/c_{pg})/\rho_L$ [32]. The conductive heat flux from the flame to the droplet surface is strongly dependent on the gas thermal conductivity.

To ensure a high level of accuracy, the property database adopted for the simulations (based on the Chapman-Enskog kinetic-theory) was tested against experimental thermal conductivity data available for pure fuel components, with ad-hoc corrections made to improve agreement with the experimental conductivity data. Concerning the liquid mixture model, previous simulations have shown that the assumption of ideal mixtures for the gas phase is adequate for combustion at atmospheric pressure. Non-negligible deviations from the ideal behavior were observed only at high pressure (>40 atm) but the flexibility exists to incorporate an equation of state for property predictions if necessary.

4.2. Radiation heat transfer model

Radiation can have a strong impact on droplet burning especially for large droplets greater than about 2 mm burning in the standard atmosphere. The radiative heat flux for the energy equation was evaluated on the basis of the P1 model of [33] which represents a good compromise between computational load and accuracy. The absorption coefficient α_p of the absorbing (radiating) gas and soot was calculated as the sum of the absorption coefficients of pure gas α_g and pure soot α_s using the gray-medium model. We assumed that H_2O, CO, CO_2 and CH_4 were the only significant gaseous absorbing (radiating) species and α_s was expressed as

$$\alpha_g = p_{H_2O}\alpha_g^{H_2O} + p_{CO}\alpha_g^{CO} + p_{CO_2}\alpha_g^{CO_2} + p_{CH_4}\alpha_g^{CH_4} \tag{1}$$

where p_k are partial pressures of species k. The absorption coefficients α_g^k of species k were estimated from calculations based on software reported in [34]. The soot contribution was calculated according to the correlation proposed [35],

$$\alpha_s = (b_1 + b_2 T) f_v \tag{2}$$

where $b_1 = -1.23 \times 10^5$ m^{-1} and $b_2 = 572$ K^{-1}m^{-1}. More accurate approaches, such as the weighted-sum-of-gray-gases (WSGG) model [36] or the statistical narrow band (SNB) model adopted in [37] may improve the predictive capabilities of the simulations and will be explored in future work.

4.3. Diffusion in liquid phase

The treatment of diffusion fluxes of species in the liquid phase is important to predict the temporal distribution of species in the droplet including water dissolved at the droplet surface that diffuses into the interior. Diffusion fluxes in the liquid phase were described by the Stefan-Maxwell theory [38]. In radial coordinates, molar diffusion fluxes $\boldsymbol{J_L}$ for N_L liquid species (=7) are given by

$$\boldsymbol{J}_L = -C_L^{tot}\boldsymbol{B}^{-1}\boldsymbol{\Gamma}\frac{\partial \boldsymbol{X}}{\partial r} \tag{3}$$

where C_L^{tot} is the liquid-phase concentration and $\frac{\partial X}{\partial r}$ represents the radial gradients of mole fractions of the species. The elements of the $\boldsymbol{B}$ matrix are

$$B_{ij} = -X_i\left(\frac{1}{\Lambda_{ij}} - \frac{1}{\Lambda_{in}}\right) for\ i \neq j \tag{4}$$

and

$$B_{ii} = \frac{X_i}{\Lambda_{in}} + \sum_j^{N_L}\frac{X_j}{\Lambda_{ij}} \tag{5}$$

The Λ_{ij} are Stefan-Maxwell binary diffusion coefficients [39],

$$\Lambda_{ij} = \left(\Lambda_{ij}^0\right)^{\frac{1+x_j-x_i}{2}}\left(\Lambda_{ij}^0\right)^{\frac{1+x_i-x_j}{2}} \tag{6}$$

and Λ_{ij}^0 are the infinite dilution binary coefficients for species i and j. These are evaluated using the correlation in [40]. $\boldsymbol{\Gamma}$ is the activity matrix with elements

$$\Gamma_{ij} = \delta_{ij} + X_i\frac{\partial ln\gamma_i}{\partial X_j}\bigg|_{T,P,X_{k\neq j=1,2,\ldots N_L-1}} \tag{7}$$

where δ_{ij} is the Kronecker delta function. γ_i are the activity coefficients of

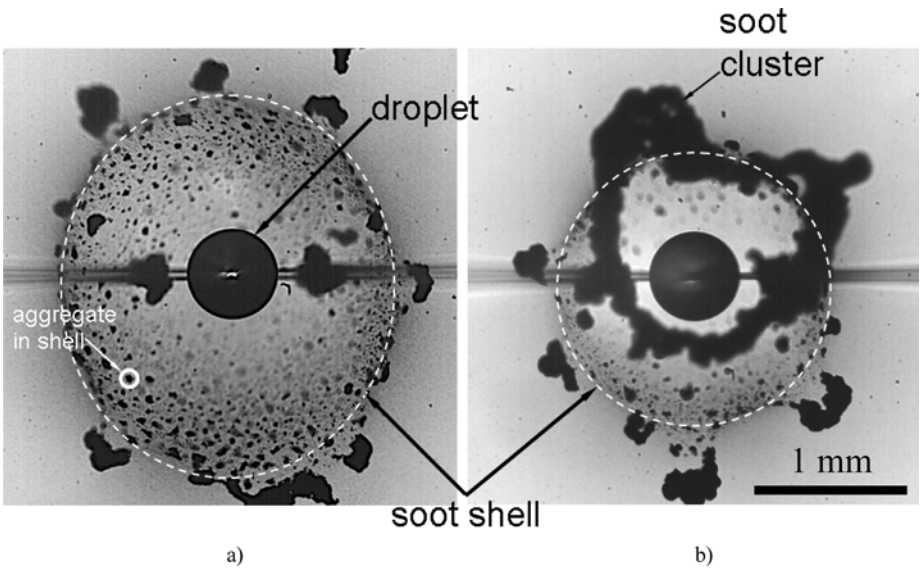

Fig. 3. Selected photographs from Fig. 1 of burning pumpE10 (a) and S3 (b) droplets at 0.4 s/mm^2. The elliptical boundaries (dotted lines) show the soot shell as determined by the user. Individual aggregates are part of the soot shell while soot clusters are not. Support fibers (blurred) are visible.

species i evaluated through the UNIFAC approach [41]. $\boldsymbol{J_L}$, $\boldsymbol{B}$ *and* $\boldsymbol{\Gamma}$ are of order N_L-1 because the last (i.e. N_L) diffusion flux is not independent but is evaluated via the flux closure condition,

$$J_{L,N_L} = -\sum_{i=1}^{N_L-1} J_{L,i} \tag{8}$$

4.4. Thermodynamic equilibrium

To account for deviations from ideal mixture behavior in the S3 droplet and to determine surface mass fractions, a modified version of Raoult's law was adopted. For each of the species *i* in the liquid phase,

$$p_i\phi_i = X_i p_i^v \gamma_i \tag{9}$$

where p_i is the partial pressure of the vapor, ϕ_i is the fugacity coefficient in the gaseous phase, X_i is the mole fraction in the liquid phase, p_i^v is the vapor pressure of pure species i and γ_i is the activity coefficient in the liquid phase. Gas phase non-ideality was neglected (i.e. $\phi_i = 1$) whereas liquid phase mixture non-idealities were accounted for by non-unity activity coefficients γ_i. Non-negligible deviations from ideal liquid mixture behavior (e.g., which could be addressed using a cubic equation of state) may be expected only at high pressure (>40 atm).

4.5. Kinetic mechanism

The reactions scheme for oxidation and pyrolysis of the S3 surrogate was taken from the POLIMI 1909 mechanism [8]. It consists of 398 species and 24,814 reactions and includes soot chemistry, described via a discrete sectional method, accounting for nucleation, surface growth, coalescence/aggregation, and oxidation of soot particles. The POLIMI mechanism is robust enough to enable predictions of soot precursor and greenhouse gas species such as acetylene and carbon dioxide and a range of other species. The fact that the POLIMI-1909 mechanism worked reasonably well for simulating S3 droplet burning (as noted in Section 5) now makes it a good system on which to reduce

the number of reaction steps in order to improve computational time for S3 combustion simulations. Mechanism reduction was not carried out for the present study.

The need to incorporate a kinetic mechanism with such a large number of miscible species as the S3 surrogate was due to considerations of soot formation and the many polycyclic aromatic hydrocarbon (PAH) molecules that contribute to it. A prior study [17] incorporated an earlier version of this mechanism with fewer species and reactions to simulate droplet burning of a single component hydrocarbon with soot formation (n-heptane) with reasonably good success. The POLIMI kinetic mechanism includes reactions relevant to a wide range of conditions (low, intermediate and high temperature conditions, low and high pressure, lean to rich and diluted conditions). For the highly multicomponent S3 mixture we did not have justification for reducing this mechanism prior to its use in predicting S3 droplet. Mechanism reduction is an effort for future work. Uncertainties of kinetic rate parameters are also factors that influence predictions and this matter has been discussed for the POLIMI mechanism in [42].

The POLIMI mechanism is based on the Aramco C0–C2 mechanism [43] combined with the C3 subset from [44] with additional blocks of reactions added in a modular fashion to describe the chemistry of heavier components according to a hierarchical structure [45]. The mechanism also includes specific modules that include the formation and oxidation of mono-aromatic and polyaromatic hydrocarbons (PAH) as reported in [46,47] which are involved in processes related to forming particulate matter during droplet burning. The modular approach, which combines detailed and lumped chemistry, can describe the reactivity of complex fuel blends in a wide range of conditions, limiting at the same time the total number of chemical species involved, which is an advantage when simulations require a tight discretization of the spatial domain. The mechanism has been previously tested against experimental configurations very different from the droplet flame. The configurations employed pre-vaporized fuel with a 0-D or 1-D transport.

The original mechanism did not include the combustion chemistry of cyclo-pentane which is one of the S3 components. This species was added to the mechanism with high temperature reactions and parameters from [48]. Cyclo-pentane is peculiar among cyclo-alkanes because of its propensity to dehydrogenate via a sequence of abstraction reactions followed by O2 addition and elimination to form cyclo-pentene. This feature inhibits the development of low temperature branching paths and is responsible for the high-octane number sensitivity of this fuel. Moreover, the cyclo-pentene resulting from this process is rapidly abstracted to form cyclo-pentadienyl radicals which is a chemical species conducive to the formation of PAHs involved in soot production.

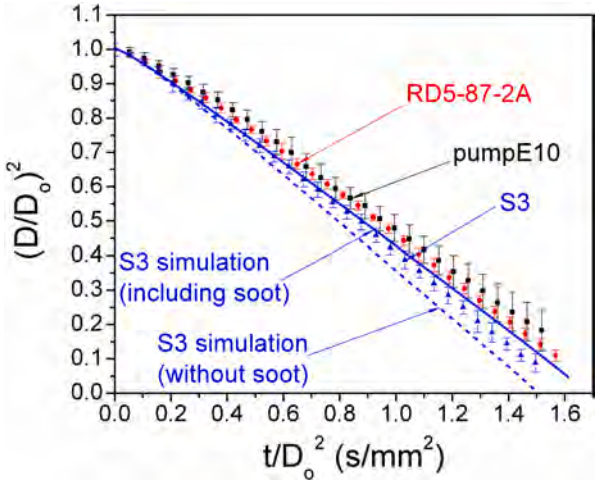

Fig. 4. Evolution of $(D/D_o)^2$ averaged over four experimental runs with a scaled time for RD5-87-2A, S3, and pumpE10. The lines are from simulations which include soot (solid) and which do not (dashed). The experimental data shown are given in the SM2 section.

4.6. Soot model

Formation of soot was modeled using the methodology reported in [46,49]. Heavy PAHs (MW $\leq$ 3000 g/mol) and particle sizes were discretized into 25 classes of pseudo-species (called BINs) with their masses doubled from one class to the next. Each class was represented by lumped pseudo-species (BINs) with fixed numbers of carbon and hydrogen atoms. Thermochemical properties of the pseudo-species BINs were based on the group additivity method. PAHs of more than 20 carbon atoms constituted the first 4 BINs. These species were defined as heavy PAHs in contrast to light PAHs up to pyrene, which are considered in the gas-phase model.

The first soot particles were modeled as a cluster containing 320 carbon atoms and were classified into BIN5. Although the choice for the first soot particles may be arbitrary, the threshold assigned is consistent with the observation of heavy PAHs extracted from flame-generated soot [50] and with recent measurements [51]. Particle shapes for BIN5 to BIN12 were assumed to be spherical with a particle mass density of 1.5 g/cm^3 [52]. BIN12 consisted of particles with diameters of ~10 nm and this BIN size served as the primary particle from which aggregates in larger BINs are formed.

BINs 13 to 25 were assumed to be monodisperse nonspherical aggregates or mass fractals containing a number of BIN12 primary particles. The fractal dimension was assumed to be 1.8 based on values reported for nascent soot formed in a series of premixed ethylene flames [53] and for very rich sooting flames [54]. Dehydrogenation may occur as soot grows and ages. In general, hydrogen content decreases with an increase in soot mass due to both the conversion of PAHs into more peri-condensed rings and their progressive de-alkylation. Three H/C ratios were considered for particles up to BIN10, while only two hydrogen levels were assumed for heavier BINs.

The different BINs interact with gaseous species and each other via heterogeneous pseudo-reactions. Six reaction classes were considered: i) Hydrogen-Abstraction-Carbon-Addition (HACA) mechanism; ii) inception; iii) surface growth; iv) dehydrogenation; v) coalescence and aggregation; vi) oxidation. Each of these heterogeneous processes was described with respect to analogous gas-phase reactions, which served as a reference. The reference kinetic parameters are available in [46,49].

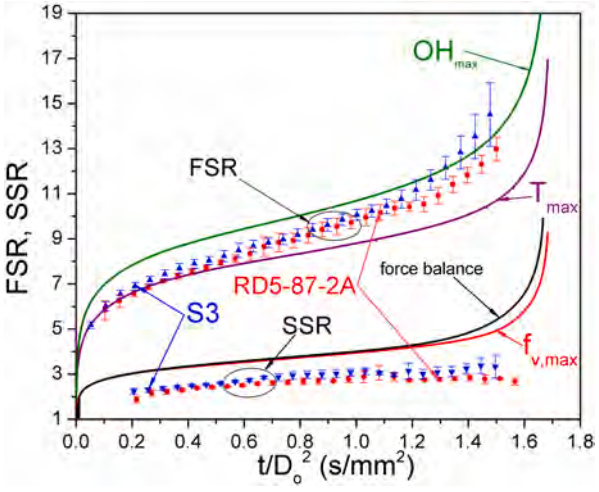

Fig. 5. Evolution of FSR and SSR with a scaled time for S3 and RD5-87-2A averaged over four experimental runs. FSR simulations are based on a flame location defined by an OH_{max} concentration or maximum gas temperature, T_{max}. Solid lines are results from simulations of S3 only. Soot shell predictions are shown based on a force balance on aggregates. The experimental data shown are given in the SM2 section.

5. Comparisons with experiments and simlations

5.1. Experimental comparisons of S3 surrogate with RD5-87-2A and E10

Fig. 1 shows representative photographs of selected burning sequences of S3, RD5-87-2A and pumpE10 droplets. The photographs illustrate both flame-illuminated and back-lighted black and white (BW) images. From a qualitative perspective, the images do not show strongly differentiated flame luminosities and sooting patterns. The flame brightness, which is qualitatively indicative of soot formation [55], appears to be roughly the same for the three fuels.

Initially, a spherical-like pattern of soot is formed as noted by the black ring-like structures which are the soot shells. The shell diameters decrease with the droplet diameter. Soot particles coalesce during burning and form larger clusters that are not as controlled by the forces on them as individual and smaller clusters formed earlier in the burning process. In the presence of these clusters there is an underlying shell visible in the images (e.g., 0.4 s for S3 in Fig. 1). This is shown in Fig. 3.

The most convincing way to assess if a surrogate mimics the fuel for a particular combustion configuration is to burn the surrogate and fuel in the same combustion configuration and under the same conditions, and to compare the results. Figs. 4 and 5 show such a comparison. The average of four experimental runs are shown with standard deviations indicated in both figures. The lines are from the simulations which are discussed in Section 5. In Fig. 4 the droplet diameter is non-dimensionalized by D_o and time is scaled as t/D_o^2. In Fig. 5 the relative positions of the flame and soot shell diameters to the droplet are shown, D_f/D and D_s/D, respectively (also termed the 'flame standoff ratio' (FSR) and the 'soot standoff ratio' (SSR)). The experimental data in Figs. 4 and 5 are provided in the Supplementary Material Section (SM2) of the paper.

Figs. 4 and 5 show very good agreement of the data for S3 and RD5-87-2A for the evolution of droplet, flame and soot shell diameters. This agreement confirms the value of the S3 mixture as a viable surrogate for RD5-87-2A for the configuration of the one-dimensional droplet burning configuration. The pumpE10 burn rates (i.e., derivatives or slopes of the data) are also in good agreement though with slightly lower values. The small differences late in the burning process could indicate the need for finer adjustments to the surrogate composition. In view of Figs. 4 and 5, surrogates developed using traditional targets (e.g., C/H ratio, RON, MON, mixture molecular weights, distillation curve, liquid density,

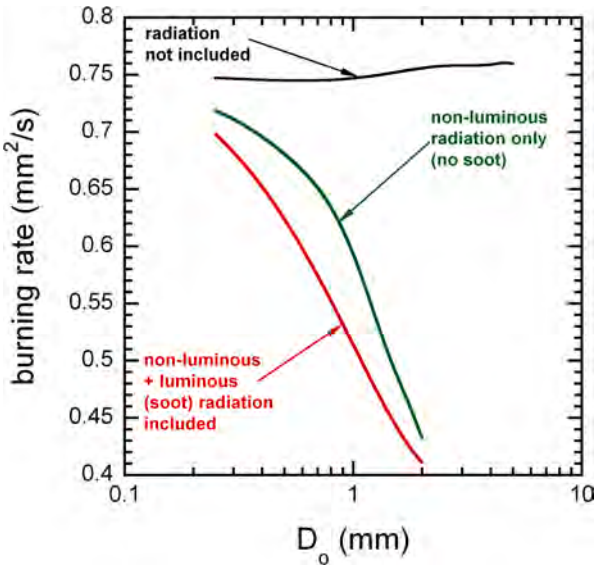

Fig. 6. Variation of simulated droplet burning rate with initial droplet diameter including flame radiation (with or without luminous emission) or excluding it in the model.

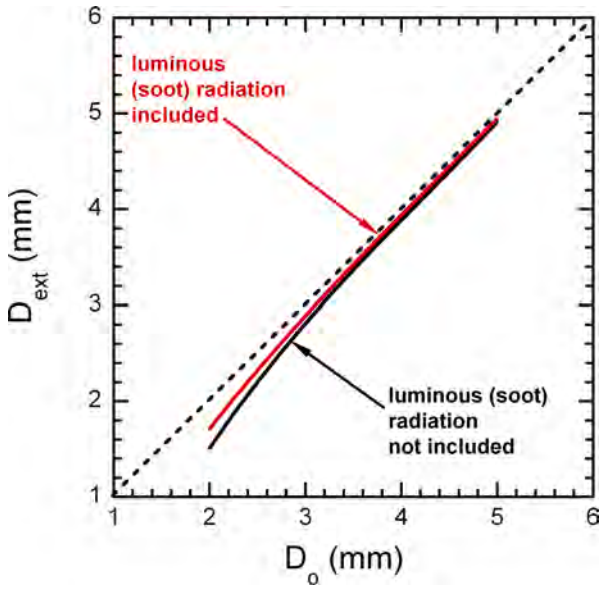

Fig. 8. Variation of simulated extinction diameters with initial droplet diameter including flame radiation (with or without luminous emission) or excluding it in the model.

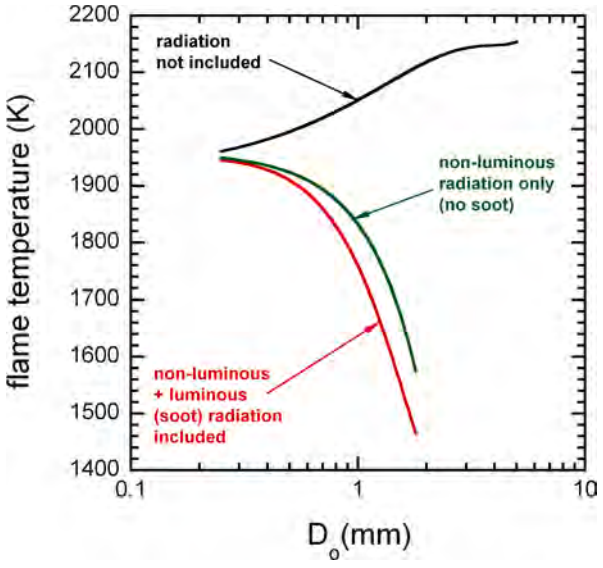

Fig. 7. Variation of simulated flame temperature (defined by T_{max}) with initial droplet diameter including flame radiation (with or without luminous emission) or excluding it in the model.

cetane number, threshold sooting index, etc.) may have broader applicability to multiphase combustion configurations.

5.2. Comparison with simulations

Figs. 4 and 5 show that predicted droplet combustion properties are in good agreement with measurements. From Fig. 4, it is evident that the agreement between simulation and experiment is quite satisfactory. Adjustments a posteriori either in the kinetic mechanism or in the calculation of transport properties of chemical species (gaseous and liquid phases) were not made to achieve this agreement. The simulated system is complex, not only from a kinetic point of view but also from the physical property point of view because of the interconnectedness of several phenomena, including (radial) convective and diffusion transport, thermodynamic equilibrium, vaporization, radiation, and soot formation. Some simplifications in the model are, though, unavoidable such as the treatment of the liquid mixture and the luminous contribution of soot to radiative heat transfer. Discrepancies between the model and the experimental data cannot entirely be avoided.

Fig. 4 also shows a simulation where radiation is removed entirely from the numerical simulation. The droplet is predicted to burn considerably faster. This higher burn rate is the result of the higher flame temperature that results when radiative looses are absent. The relation between radiation and flame temperature is discussed in Section 6.

Regarding the droplet flame, no obvious flame diameter emerges from the simulations because the gas field is fully simulated and no approximations are made about the reaction zone (e.g., such as the 'flame-sheet' approximation). Two possibilities for a flame diameter were considered: maximum temperature; and peak OH concentration. Fig. 5 shows that the peak gas temperature represents the FSR early in the burning process. Later in burning the peak OH concentration better matches the flame diameter.

Predictions of the soot shell diameters are shown in Fig. 5. The soot shell diameter is defined as the diameter where forces on the aggregates balance. The trends are consistent with the data though higher. Fig. 5 shows that the predicted soot shell diameters based on a force balance coincide with the predicted diameters based on the maximum soot volume fraction. Given the challenges of measuring the flame and soot shell diameters which are based on user-defined boundaries in the photographs, the simulations do a very respectable job of predicting trends in the evolution of flame and soot shell diameters.

6. Discussion of results

Thermal processes that influence the fuel burn rate include heat conduction (Q_c) from the flame to the droplet and radiant heat loss from the flame to the far-field (Q_{rad}). For heat conduction, $Q_c \propto (T_f - T_d)/[D(FSR-1)]$. For radiant heat loss from the droplet flame, $Q_{rad} \propto D_f^3 T_f^4$ [56]. The flame temperature depends on droplet diameter as well as the nature of the radiative transport mechanism (from luminous soot incandescence or non-luminous (no soot)

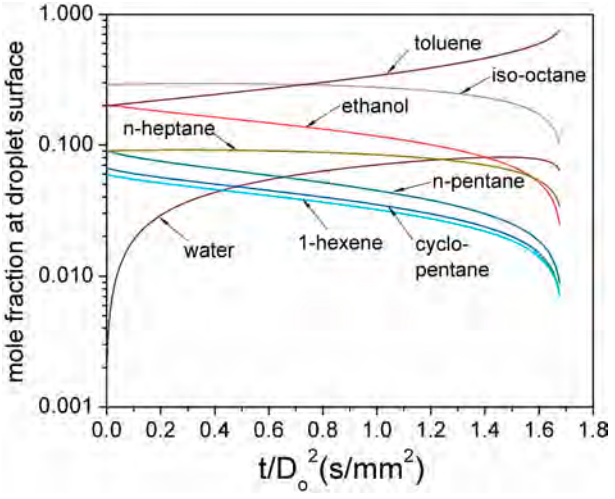

Fig. 9. Evolution of S3 component concentrations (mole fractions) at droplet surface. Initial concentrations (at 0.0) are listed in Table 1. Water at the surface is due to condensation on the droplet.

emissions). The FSR increases (Fig. 5), while T_f decreases as shown in Fig. 6 when radiation is included in the simulation. The burning rates in Fig. 6 were obtained from simulations like those shown in Fig. 4 by linearizing the evolution of $(D/D_o)^2$ between $(D/D_o)^2 = 0.30$ and $(D/D_o)^2 = 0.80$. Including luminous radiation lowers substantially the burning rate compared to non-luminous radiation which is always present. Comparing Figs. 6 and 7 suggests that T_f will be the most important variable that influences heat transfer and the burning rate.

The trends in Fig. 7 provide clues to the mechanisms influencing the variation of flame temperature with D_o. Heat loss from the flame and the flame's strain rate are important considerations. With increasing D_o radiative heat transport from the flame increases and the flame temperature would decrease. At the same time, the flame strain rate is inversely proportional to D_o^3 and lower strain rate flames have higher flame temperatures. As shown in Fig. 7, when flame radiation is not included the flame temperature indeed increases as D_o increases which is consistent with a strain rate effect. However, with radiation the opposite trend is found namely that the flame temperature decreases with increasing D_o which is explained by the dominance of a radiant heat loss mechanism on flame temperature with increasing D_o. When radiation is neglected entirely in the analysis, Fig. 6 shows that the burnsize as D_o decreases. This trend is consistent with an earlier numerical simulation of n-heptane droplet burning that included a complex chemical mechanism for fuel oxidation but neglected radiation entirely [57] and no influence of D_o was found from the simulations. This trend also follows the classical theory of droplet burning [32] which does not consider radiation and which predicts no dependence of droplet size on the burning rate.

For $0.25\,\text{mm} \leq \text{Do} \leq 1.8\,\text{mm}$ the S3 droplets burned to completion. Smaller droplets evaporated too rapidly before ignition could occur. For larger droplets, Fig. 8 shows simulated extinction diameters that are almost coincident with initial droplet diameters and the droplets extinguished also immediately after being ignited. The influence of luminous radiation is small with droplets having a slightly larger extinction diameter when luminous radiation is included.

The experimental results of Figs. 4 and 5 do not show an obvious preferential vaporization effect as characterized by a sequential vaporization of components. Such an effect could be revealed in the coordinates of Figs. 4 and 5 if there were significant differences in component properties but this does not seem to be the case for the property values in Table 1. The evolution of droplet surface compositions and spatio/temporal distribution of species in the droplet interior would provide more direct evidence for this potential.

Fig. 9 shows the evolution of the S3 component concentrations at the droplet surface. The concentrations sum to unity at any time and the initial concentrations (time zero in Fig. 9) are listed in Table 1. The components evaporate at different rates. This is seen by the time-dependenceof the surface mole fractions. Toluene is the most non-volatile component, it is slow to evaporate, and it accumulates at the surface. The other components evaporate and their surface concentrations decrease. Iso-octane has the highest concentration initially and its concentration is nearly uniform for about the first half of burning. Later in burning the surface concentration of iso-octane decreases and the toluene concentration increases. Near the end of burning, the droplet becomes almost entirely comprised of toluene.

To explore the possibility of preferential vaporization where the data in Fig. 4 do not clearly show this process, simulations were performed to predict the spatio/temporal distributions of mixture components in the droplet. Fig. 10 shows results for toluene, ethanol, n-pentane and iso-octane droplets at three different scaled times after ignition for a given droplet. The SM1 section includes similar results for the remaining three surrogate components, n-pentane, 1-hexene and cyclo-pentane. The color bars in the last column indicate the droplet composition. While Fig. 9 shows surface concentrations over the entirety of the droplet burning history, Fig. 10 shows concentrations over the entirety of the droplet interior for three selected times. The surface concentrations for the simulations in Fig. 10 at the three times shown can be inferred from the color chart in the last column of Fig. 10. The color-coded concentration values for the droplet surface are consistent with Fig. 9 and Table 1. The transition across color gradients in Fig. 10 is due to diffusion boundary layers inside the droplet across which concentrations change from interior to surface values. These layers form quickly after ignition and their sizes depend on the liquid diffusion coefficient.

During burning the droplet surface is depleted of most components except toluene while the interior concentrations do not change much as shown in Fig. 9 due to the low diffusion coefficients. In such a circumstance volatile components remain inside the droplet. If the droplet temperature is high enough a flash boiling or 'microexplosions' effect can occur by the nucleation of bubbles inside the droplet. The threshold temperature to trigger such an effect is determined by the mixture fractions of the components and their properties [58].

The potential for flash boiling can be assessed by comparing the highest droplet temperature possible at any time during burning with the homogeneous nucleation temperature of the most volatile mixture component. For many organic liquids at atmospheric pressure, homogeneous nucleation is typically initiated at $T/T_c \approx 0.90$ at atmospheric pressure. For example, n-pentane has the lowest homogeneous nucleation temperature which from experiments at atmospheric pressure has been shown to range between 418 K and 424 K [59]. Droplet temperature is the key trigger. The computed evolution of droplet surface temperature is shown in Fig. 11. With the highest wet-bulb (droplet) temperature of about 370 K and bubble point temperature of 380 K, the droplet temperature is too low to trigger a flash boiling event for pure n-pentane by homogeneous nucleation for the S3 mixture. However, when considering droplets in contact with SiC fibers the potential for internal bubbling is enhanced.

The energetic threshold for bubble nucleation of a liquid in contact with a solid surface (heterogeneous nucleation) is lower than in the bulk (homogeneous nucleation) due mainly to a contact angle effect that truncates the bubble volume and lowers the energy of forming a bubble by random density fluctuations. The nucleated bubble will grow, and as it does the droplet could appear to become larger in size as the bubble expands. At the same time, liquid evaporation can compensate and lead to a situation where the droplet diameter itself appears not to change early in burning. This effect was infrequently observed in the experiments.

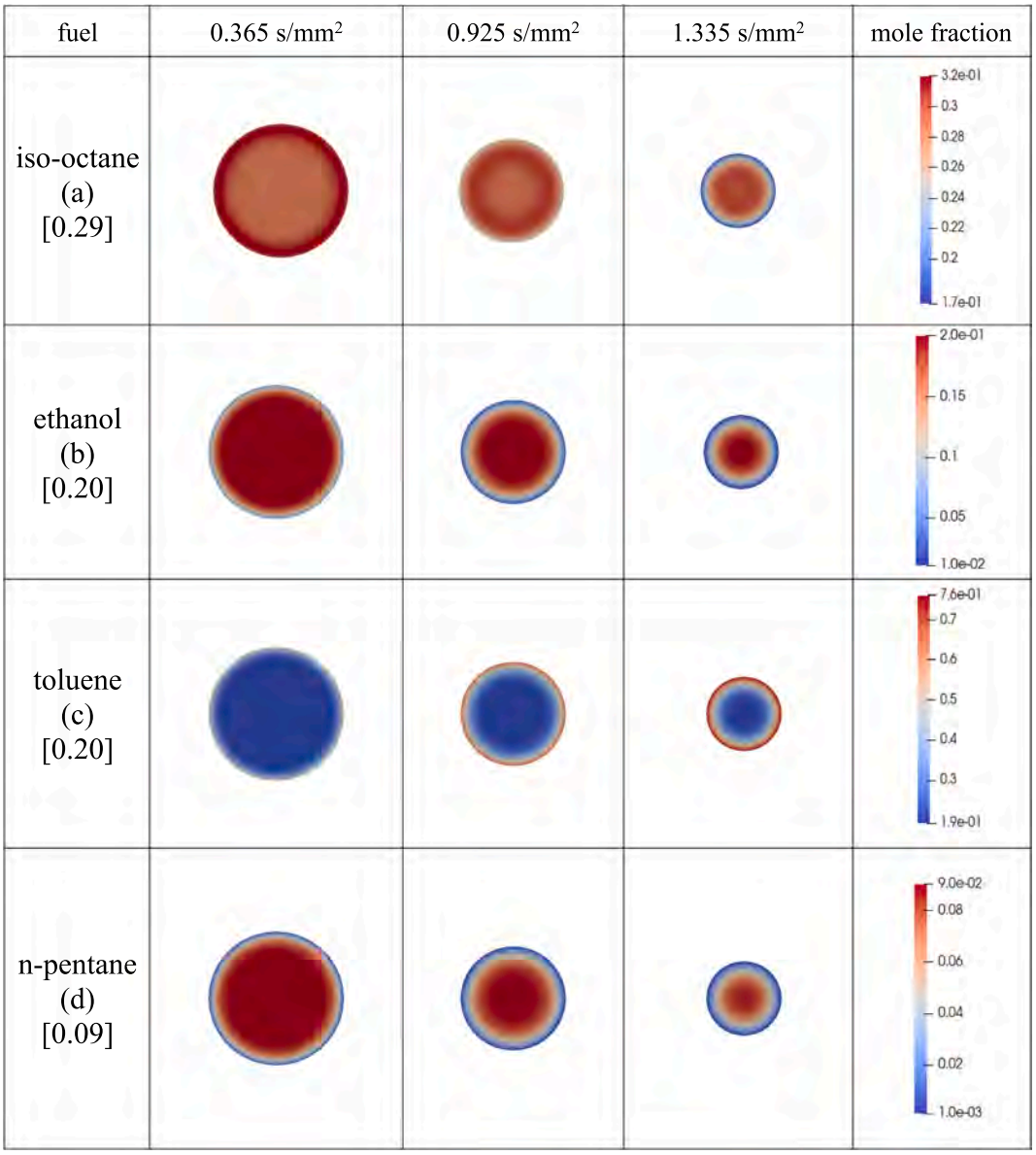

Fig. 10. Scale images showing the evolution of liquid mixture fractions of selected S3 components for three times after ignition ($D_o = 0.63$ mm) for the same droplet. Numbers in brackets in the first column are the initial concentrations (mole fraction) in the droplet. Vertical bars in the last columns show the color-coded mole fractions for each component. Fig. 9 shows the evolution of surface concentrations.

Simulations of the evolution of gas temperature, OH concentration, radiative heat transfer field and soot volume fraction are shown in Fig. 12. For purposes of this discussion the flames and soot shells are taken as corresponding to T_{max} and f_{vmax}, respectively. The dotted lines correspond to the flame and soot shell based on these definitions. Fig. 12a shows the distribution of gas temperature in relationship to the soot shell. The shell is seen to reside in the temperature range between 1300 K and 1400 K which is close to the soot inception temperature [60] for diffusion flames. Specific values depend on the experimental procedure, combustion configuration and fuel type. The OH concentration field in Fig. 12b follows the peak gas (or flame) temperature shown in Fig. 5.

The total radiant energy field – combined luminous and non-luminous – is shown in Fig. 12c. The simulations show that radiant emissions are concentrated between the flame and soot shell. As emissions qualitatively correlate with the 'brightness' of an image (Fig. 1), the field of view can be overwhelmed by radiant emissions and mask other features such as the flame itself. Fig. 12c suggests this possibility. For this reason the boundary of the brightness of a burning droplet will not always be a good measure of the actual flame diameter. The soot volume fraction is concentrated well inside the flame as expected and shown in Fig. 12d, and also coincides with f_{vmax}. This is not surprising since where the soot aggregates are trapped should have the highest concentration of soot.

Acetylene is an important soot precursor species. Virtually no acetylene should be found at the flame or far field because acetylene forms by thermal decomposition inside the flame and ultimately is transformed into soot. This is consistent with the simulations in Fig. 13a. As fuel evaporates, it flows outward and is progressively heated as it approaches the high temperature region near the flame. The fuel pyrolyzes inside the flame where soot precursors are transformed into solid aggregates. While acetylene is concentrated inside the flame and diffuses toward and away from the soot shell, CO_2 only forms at the flame so its concentration will be highest there. Fig. 13b shows this to be the case

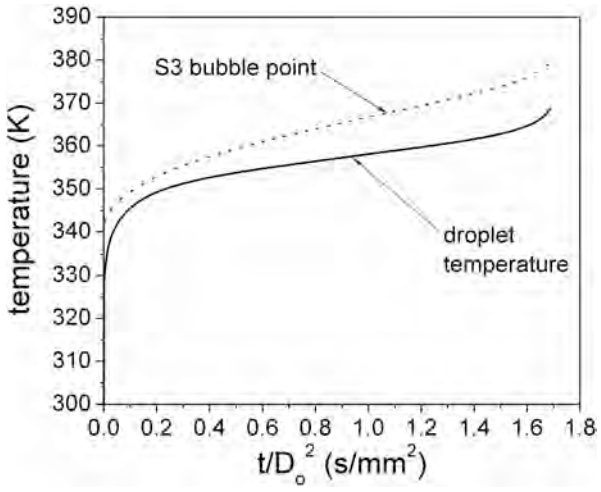

Fig. 11. Evolution of droplet surface (wet bulb) temperature and the S3 bubble-point temperature corresponding to the surface concentrations in Fig. 9.

The CO_2 concentration decreases toward the droplet and away from the flame.

Other soot precursor species to consider in forming particulates are benzene (C_6H_6), naphthalene ($C_{10}H_8$), indene, fluorene, large PAH molecules, etc. Considering in particular large PAH molecules (i.e., those with >4 aromatic rings), Fig. 13c shows the evolution of PAH in relation to the maximum soot volume fraction and flame temperature. The simulations show that the PAH concentration is highest near to the maximum soot volume fraction where the soot shell resides.

The numerical analysis included water vapor condensation on the droplet surface. During burning water vapor formed at the flame diffuses to the droplet where it condenses on the droplet surface and dissolves in the ethanol there. The concentration of water at the droplet surface increases. Fig. 14 shows the influence of water condensation on the evolution of droplet diameter (14a), FSR (14b) and SSR (14c).

It has been considered that water condensation enhances the fuel evaporation rate by the added energy from the release of the enthalpy of condensation [19]. For the conditions reported here, Fig. 14a shows no effect of water condensation on S3 droplet burning. Similarly, the flame and soot shell diameters show only the barest evidence of a water condensation effect. From Fig. 14b and 14c, the flame and soot shells move slightly closer to the droplet when a water condensation process is included in the numerical model.

7. Conclusions

The combustion of a surrogate fuel for E10 was studied experimentally and numerically for the configuration of an isolated droplet burning under conditions with no externally imposed convection from buoyancy or forced flow. The experiments were carried out for droplets with $D_o = 0.63$ mm burning in the standard atmosphere. The experimental results showed very good agreement among the three fuel systems examined for the burning rate and the evolutions of droplet, flame and soot shell diameters. No targets specifically connected with the liquid phase were included in developing the surrogate. Numerical simulations for the surrogate showed good agreement with experimental data for these same variables.

Simulations were also carried out to examine the influence of radiation from both luminous and non-luminous contributions and the initial droplet size on the droplet burning rate, flame extinction diameter, and water condensation for 0.25 mm $\leq D_o \leq$ 5 mm. The influence of

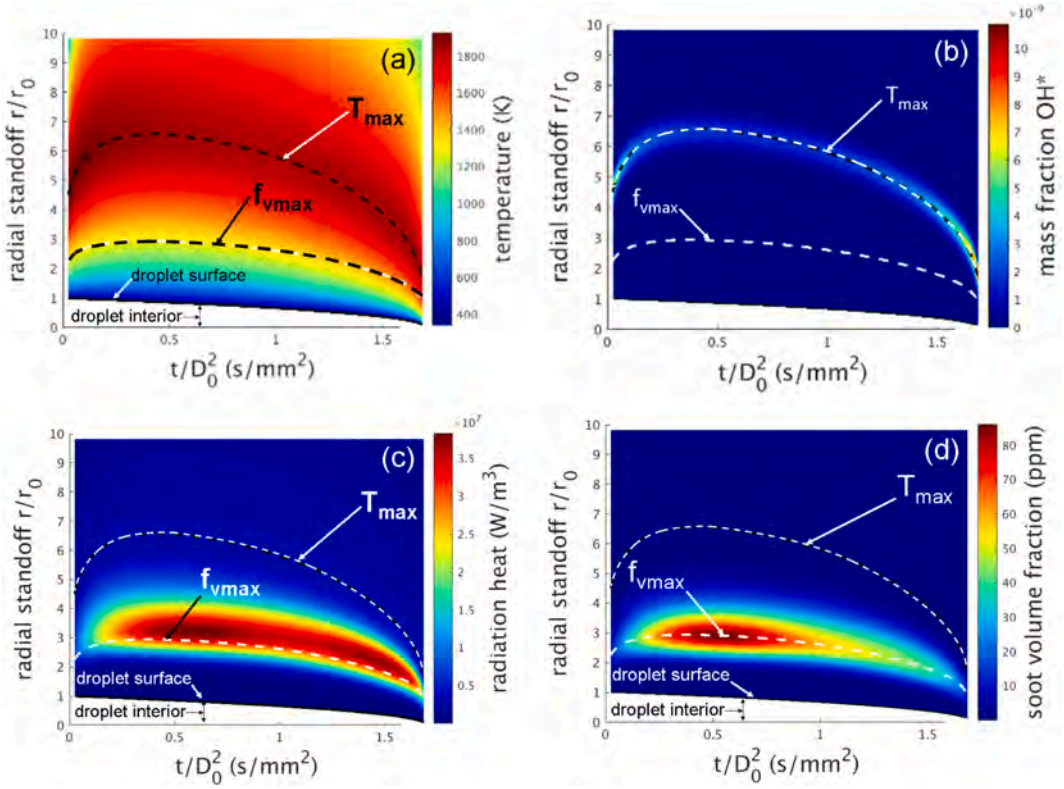

Fig. 12. Color maps showing simulations of gas temperature (a), distribution of OH radicals (b), radiant emissions (c) and soot volume fraction (d) in relation to the flame, soot shell and droplet surface.

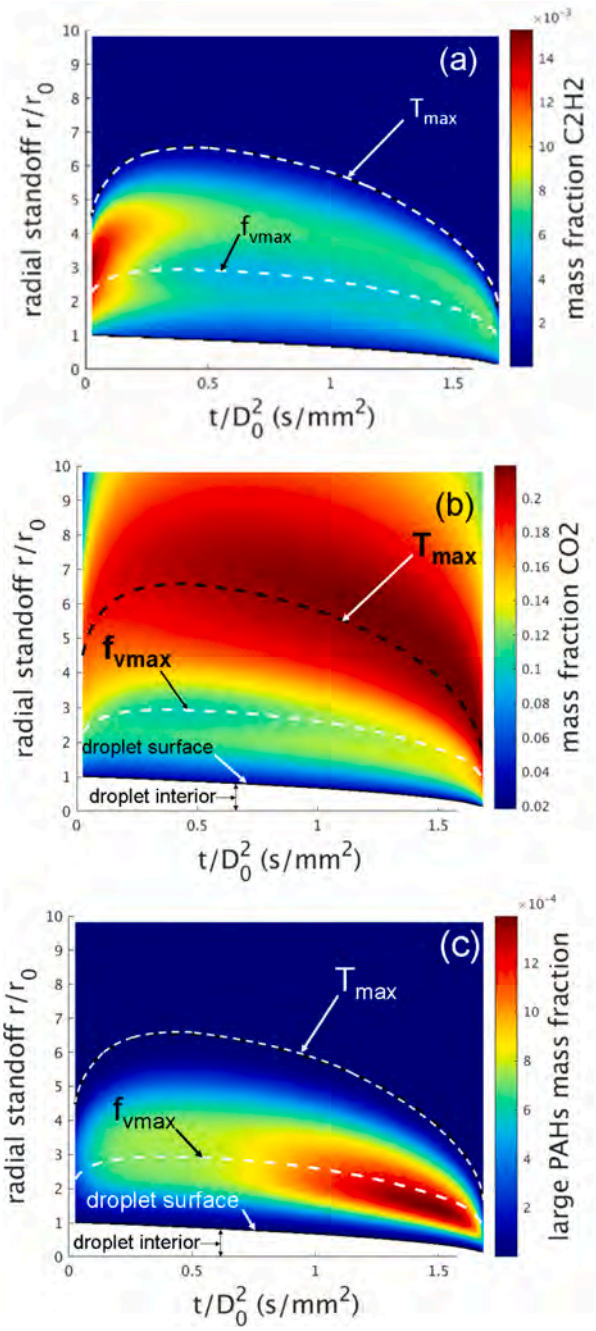

Fig. 13. Distribution of acetylene (a), CO_2 (b) and large PAH molecule (c) concentrations in relation to the soot shell, flame, droplet surface.

water condensing on the droplet surface was small over this range. Radiation strongly influenced the burning rate for $0.25\ \text{mm} \leq D_o \leq 2\ \text{mm}$ with droplets burning slower as D_o was increased. The radiation effect was more pronounced when a luminous component of radiation due to soot incandescence was added to the intrinsic non-luminous radiation that is always present. Entirely removing radiation in the simulations resulted in burning rates becomming and resulting in an asymptotic value for a small-droplet limit.

Below 0.25 mm, droplets evaporated too quickly to be ignited for the numerical parameters of the ignition source and radiation was negligible. Droplets larger than $D_o = 2.0$ mm showed a strong radiation effect as they extinguished almost immediately upon ignition and transitions to cool-flame behavior were not observed for the surrogate. Preferential vaporization was not clearly revealed in the experimental data while simulated internal droplet concentrations showed evidence of this effect by development of concentration boundary layers inside the droplet. Droplet concentrations were not generally conducive to promoting flash boiling as triggered by an internal nucleation mechanism for the surrogate components and flash-boiling was rarely observed.

CRediT authorship contribution statement

Alberto Cuoci: Conceptualization, Data curation, Formal analysis, Investigation, Software, Writing - original draft, Validation. **C. Thomas Avedisian:** Formal analysis, Conceptualization, Data curation, Investigation, Project administration, Software, Supervision, Validation, Writing -

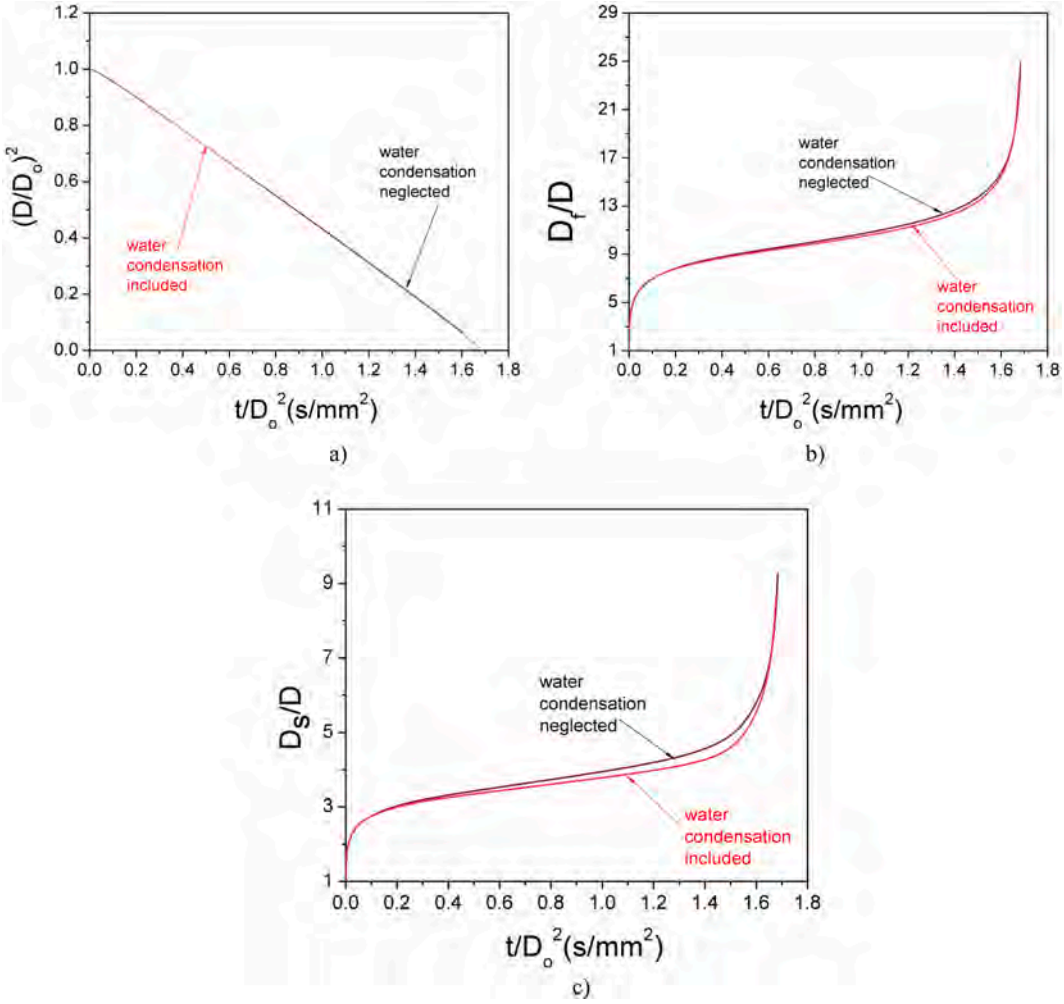

Fig. 14. The influence of water condensation on burning for a $D_o = 0.63$ mm S3 droplet for a) droplet diameter, b) flame standoff distance (D_f/D), and c) soot shell standoff distance (D_s/D).

original draft. **Jordan D. Brunson:** Data curation, Investigation, Methodology, Visualization, Writing - original draft. **Songtao Guo:** Data curation, Investigation, Methodology, Visualization. **Alireza Dalili:** Data curation, Investigation, Methodology, Visualization. **Yujie Wang:** Data curation, Investigation, Methodology, Visualization. **Marco Mehl:** Investigation, Methodology, Validation, Writing - original draft. **Alessio Frassoldati:** Formal analysis, Investigation, Software, Validation. **Kalyanasundaram Seshadri:** Formal analysis, Investigation, Software, Supervision, Validation. **John E. Dec:** Formal analysis, Investigation, Methodology, Writing - original draft. **Dario Lopez-Pintor:** Formal analysis, Investigation, Methodology, Writing - original draft.

Declaration of Competing Interest

The authors declare that they have no known competing financial interests or personal relationships that could have appeared to influence the work reported in this paper.

Acknowledgements

This work was supported by a grant from the Co-Optimization of Fuels & Engines (Co-Optima) program sponsored by the U.S. Department of Energy (DOE), Office of Energy Efficiency and Renewable Energy (EERE), Bioenergy Technologies and Vehicle Technologies Offices (grant no. DE-EE0007978) with Dr. Alicia Lindauer as the Program Manager. Additional support was received by the National Aeronautics and Space Administration (grants nos. NNX08AI51G and 80NSSC18K0480) with Dr. Michael C. Hicks as project monitor. The authors acknowledge discussions on droplet burning with Prof. Y. Xu of Prairie View A&M University, Prof. F. A. Williams of the University of California San Diego, and Profs. A. P. Reeves and P. Pepiot of Cornell. Chemical analysis of the fuel systems was carried out at Southwest Research Institute (San Antonio, TX).

Appendix A

For completeness, this appendix lists the conservation equations that were solved to simulate S3 droplet burning. The equations are presented in the spherical coordinate system. Symbols are defined in the Nomenclature section. Radiation is discussed in Section 4.2, the kinetic mechanism in Section 4.5, and the soot model in Section 4.6.

For the liquid phase ($0 < r < R_d$), the mass, energy, and species conservation equations are:

$$\frac{\partial \rho_L}{\partial t}+\frac{1}{r^2}\frac{\partial}{\partial r}\left(r^2\rho_L v_L\right)=0 \tag{A1}$$

$$\rho_L c_{p,L}\left(\frac{\partial T_L}{\partial t}+v_L\frac{\partial T_L}{\partial r}\right)=\frac{1}{r^2}\frac{\partial}{\partial r}\left(r^2 k_L\frac{\partial T_L}{\partial r}\right) \tag{A2}$$

$$\rho_L\left(\frac{\partial Y_{L,i}}{\partial t}+v_L\frac{\partial Y_{L,i}}{\partial r}\right)=-\frac{1}{r^2}\frac{\partial}{\partial r}\left(r^2\rho_L Y_{L,i}V_{L,i}\right) \tag{A3}$$

where the subscript i denotes the species in the liquid. For the gas surrounding the droplet ($r > R_d$), the one-dimensional form of the mass, energy and species conservation equations are the following:

$$\frac{\partial \rho_g}{\partial t}+\frac{1}{r^2}\frac{\partial}{\partial r}\left(r^2\rho_g v_g\right)=0 \tag{A4}$$

$$\rho_g c_{p,g}\left(\frac{\partial T_g}{\partial t}+v_g\frac{\partial T_g}{\partial r}\right)=\frac{1}{r^2}\frac{\partial}{\partial r}\left(r^2 k_g\frac{\partial T_g}{\partial r}\right)-\rho_g\sum_{i=1}^{N_g}\left(Y_{g,i}V_{g,i}c_{p,g,i}\right)\frac{\partial T_g}{\partial r}-\sum_{i=1}^{N_g}\left(\omega_{g,i}H_{g,i}\right)-\frac{\partial q_R}{\partial r} \tag{A5}$$

$$\rho_g\left(\frac{\partial Y_{g,i}}{\partial t}+v_g\frac{\partial Y_{g,i}}{\partial r}\right)=-\frac{1}{r^2}\frac{\partial}{\partial r}\left(r^2\rho_g Y_{g,i}V_{g,i}\right)+\omega_{g,i} \tag{A6}$$

where the subscript i denotes the species in the liquid. The diffusion velocities for BINs (i.e. soot pseudo-species) include also the thermophoretic velocity (see SM for additional details).

The boundary conditions are the following:

droplet center ($r = 0$):

$$v_L\big|_{r=0}=0 \tag{A7}$$

$$\left.\frac{\partial T_L}{\partial r}\right|_{r=0}=0 \tag{A8}$$

$$\left.\frac{\partial Y_{L,i}}{\partial r}\right|_{r=0}=0 \tag{A9}$$

droplet surface ($r = R_d$):

$$k_L\left.\frac{\partial T_L}{\partial r}\right|_{r=R_d^-}+\sum_{i=1}^{N_c}\left(W_{tot}Y_{g,i}+\rho_g Y_{g,i}V_{g,i}\right)h_{fg,i}=k_g\left.\frac{\partial T_g}{\partial r}\right|_{r=R_d^+}+q_R \tag{A10}$$

$$T_L\big|_{R_d^-}=T_g\big|_{R_d^+} \tag{A11}$$

$$p_i\phi_i=X_i p_i^v\gamma_i \tag{A12}$$

$$W_{tot}Y_{L,i}+j_{L,i}\big|_{r=R_d^-}=W_{tot}Y_{g,i}+\rho_g Y_{g,i}V_{g,i} \tag{A13}$$

$$W_{tot}=\rho_g\left(\nu_g-\frac{dR_d}{dt}\right) \tag{A14}$$

$r = R_\infty$:

$$T_g=T_\infty \tag{A15}$$

$$Y_{g,i}=Y_{\infty,i} \tag{A16}$$

Appendix B. Supplementary data

Supplementary data to this article can be found online at https://doi.org/10.1016/j.fuel.2020.119451.

References

[1] Gaspar DJ, West BH, Ruddy D, Wilke TJ, Polikarpov E, Alleman TL, George A, Monroe E, Davis RW, Vardon D, Sutton AD, Moore CM, Benavides PT, Dunn J, Biddy MJ, Jones SB, Kass MD, Debusk MM, Sjoberg M, Szybist J, Sluder CS, Fioroni G, Pitz WJ. Top Ten Blendstocks Derived from Biomass for Turbocharged Spark Ignition Engines: Bio-blendstocks with Potential for Highest Engine Efficiency, Report No. PNNL-28713, Pacific Northwest National Laboratory. 2019. (see also https://www.osti.gov/servlets/purl/1567705).

[2] Miles P. Efficiency Merit Function for Spark Ignition Engines: Revisions and Improvements Based on FY16–17 Research, Report No. DOE/GO-102018-5041, U. S. Department of Energy. 2018. (see also https://www.energy.gov/sites/prod/files/2018/02/f48/Co-Optima%20Merit%20Function%20Report%2067584_2.pdf).

[3] Kolodziej R, Scheib J. Bio-isobutanol: the next-generation biofuel: refining developments. Hydrocarbon Process (Int ed) 2012;91(9).

[4] Pintor DL, Dec J, Gentz G. φ-sensitivity for LTGC engines: Understanding the fundamentals and tailoring fuel blends to maximize this property. SAE World Congress Experience, April 9-11, 2019, Cobo Conference/Exhibition Center, Detroil, MI., SAE Tech. Pap..2019-01-0961, 2019.

[5] Gentz G, Dernotte J, Ji C, Pintor DL, Dec J. Combustion-Timing Control of Low-Temperature Gasoline Combustion (LTGC) Engines by Using Double Direct-Injections to Control Kinetic Rates. SAE Tech. Pap..April 2, 2019.

[6] Ekoto I, Skeen S, Steeper RR, Hansen N. Detailed characterization of negative valve overlap chemistry by photoionization mass spectroscopy. SAE Int J Engines 2016;9(1):26–38.
[7] Dec JE. Low-Temperature Gasoline Combustion (LTGC) Engine Research, Project No. ACE004, Annual Merit Review, Office of Vehicle Technologies, U.S. Department of Energy. Washington, DC, June 2018.
[8] Stagni A, Esclapez L, Govindaraju P, Cuoci A, Faravelli T, Ihme M. The role of preferential evaporation on the ignition of multicomponent fuels in a homogeneous spray/air mixture. Proc Combust Inst 2017;36:2483–91.
[9] Cuoci A, Mehl M, Buzzi-Ferraris G, Faravelli T, Manca D, Ranzi E. Autoignition and burning rates of fuel droplets under microgravity. Combust Flame 2005;143(3):211–26.
[10] Liu YC, Alam FE, Xu Y, Dryer FL, Avedisian CT, Farouk TI. Combustion characteristics of butanol isomers in multiphase droplet configurations. Combust Flame 2016;169:216–28.
[11] Marchese AJ, Dryer FL, Nayagam V. Numerical modeling of isolated n-alkane droplet flames: initial comparisons with ground and space-based microgravity experiments. Combust Flame 1999;116(3):432–59.
[12] Borghesi G, Mastorakos E. Spontaneous ignition of isolated n-heptane droplets at low, intermediate, and high ambient temperatures from a mixture-fraction perspective. Combust Flame 2015;162(6):2544–60.
[13] Liu YC, Farouk T, Savas AJ, Dryer FL, Avedisian CT. On the spherically symmetrical combustion of methyl decanoate droplets and comparisons with detailed numerical modeling. Combust Flame 2013;160(3):641–55.
[14] Xu Y, Farouk TI, Hicks MC, Avedisian CT. Initial diameter effects on combustion of unsupported equi-volume *n*-heptane/*iso*-octane mixture droplets and the transition to cool flame behavior: experimental observations and detailed numerical modeling. Combust Flame 2020;220:82–91.
[15] Kumar S, Ray A, Kale SR. A soot model for transient, spherically symmetric n-heptane droplet combustion. Combust Sci Technol 2002;174(9):67–102.
[16] Ben-Dor G, Elperin T, Krasovit B. Effect of thermo–and diffusiophoretic forces on the motion of flame-generated particles in the neighbourhood of burning droplets in microgravity conditions. Proc Math Phys Eng Sci 2003;459(2031):677–703.
[17] Stagni A, Cuoci A, Frassoldati A, Ranzi E, Faravelli T. Numerical investigation of soot formation from microgravity droplet combustion using heterogeneous chemistry. Combust Flame 2018;189:393–406.
[18] Pineda DI, Shi X, Casey TA, Chen JY. Analysis of the errors associated with molecular transport parameters in combustion modeling and their effects on one-dimensional flame simulations. in 10th US National Combustion Meeting, The Combustion Institute, College Park, MD April 23, 2017.
[19] Lee A, Law CK. An experimental investigation on the vaporization and combustion of methanol and ethanol droplets. Combust Sci Technol 1992;86:253–65.
[20] Haylett DR, Pappas PP, Davidson DF, Hanson RK. Application of an aerosol shock tube to the measurement of diesel ignition delay times. Proc Combust Inst 2009;32:477–84.
[21] Liu YC, Xu Y, Avedisian CT, Hicks MC. The effect of support fibers on micro-convection in droplet combustion experiments. Proc Combust Inst 2015;35(2):1709–16.
[22] Liu YC, Xu Y, Hicks MC, Avedisian CT. Comprehensive study of initial diameter effects and other observations on convection-free droplet combustion in the standard atmosphere for n-heptane, n-octane, and n-decane. Combust Flame 2016;171:27–41.
[23] Liu YC, Avedisian CT. A comparison of the spherical flame characteristics of sub-millimeter droplets of binary mixtures of n-heptane/iso-octane and n-heptane/toluene with a commercial unleaded gasoline. Combust Flame 2012;159(2):770–83.
[24] Reid RC, Prausnitz JM, Sherwood TK. The properties of gases and liquid. 3rd ed. New York: McGraw-Hill Book Co.; 1977.
[25] Yu J, Gou X. Comprehensive surrogate for emulating kinetic properties of jet fuels. J Propuls Power 2018;34(3):679–89.
[26] Mueller CJ, Cannella WJ, Bruno TMJ, Bunting B, Dettman HD, Franz JA, et al. Methodology for formulating diesel surrogate fuels with accurate compositional, ignition-quality, and volatility characteristics. Energy Fuels 2012;26(6):3284–303.
[27] Mehl M, Chen JY, Pitz WJ, Sarathy SM, Westbrook CK. An approach for formulating surrogates for gasoline with application toward a reduced surrogate mechanism for CFD engine modeling. Energy Fuels 2011;25(11):5215–23.
[28] Westbrook CK, Mehl M, Pitz WJ, Kukkadapu G, Wagnon S, Zhang K. Multi-fuel surrogate chemical kinetic mechanisms for real world applications. Phys Chem Chem Phys 2018;20(16):10588–606.
[29] Mehl M, Zhang K, Wagnon S, Kukkadapu G, Westbrook CK, Pitz WJ, Zheng Y, Curran HJ, Rachidi ME, Atef N, Sarathy M. A comprehensive detailed kinetic mechanism for the simulation of transportation fuels, paper No. 1A17, 10th U.S. National Combustion Meeting, Combustion Institute, College Park, M.D. April 23-29 2017.
[30] Cuoci A, Frassoldati A, Faravelli T, Ranzi E. OpenSMOKE++: an object-oriented framework for the numerical modeling of reactive systems with detailed kinetic mechanisms. Comput Phys Commun 2015;192:237–64.
[31] Dalili A, Brunson JD, Guo S, Turello M, Pizetti F, Badiali L, et al. The role of composition in the combustion of n-heptane/iso-butanol mixtures: experiments and detailed modelling. Combust Theory Model 2020. https://doi.org/10.1080/13647830.2020.1800823.
[32] Glassman I. Combustion. 3rd ed. New York: Academic Press; 1996. p. 308.
[33] Modest MF. Radiative heat transfer. Academic Press; 2013.
[34] Hall RJ. The radiative source term for plane-parallel layers of reacting combustion gases. J Quant Spectrosc Radiat Transf 1993;49(5):517–23.
[35] Hubbard GL, Tien CL. Infrared mean absorption coefficients of luminous flames and smoke. J Heat Transfer 1978;100(2):235–9.
[36] Yin C. Refined weighted sum of gray gases model for air-fuel combustion and its impacts. Energy Fuels 2013;27(10):6287–94.
[37] Farouk TI, Dryer FL. Isolated n-heptane droplet combustion in microgravity:"Cool Flames"–two-stage combustion. Combust Flame 2014;161(2):565–81.
[38] Taylor R, Krishna R. Multicomponent mass transfer. John Wiley & Sons; October 22, 1993.
[39] Wesselingh JA, Krishna R. Mass transfer in multicomponent mixtures. Delft University Press; 2006.
[40] Siddiqi MA, Lucas K. Correlations for prediction of diffusion in liquids. Can J Chem Eng 1986;64(5):839–43.
[41] Fredenslund A, Jones RL, Prausnitz JM. Group-contribution estimation of activity coefficients in nonideal liquid mixtures. AIChE J 1975;21(6):1086–99.
[42] Furst M, Sabia P, Lavadera L, Aversano G, de Joannon M, Frassoldi A, et al. Optimization of chemical kinetics for methane and biomass pyrolysis products in moderate or intense low-oxygen dilution combustion. Energy Fuels 2018;32:10194–201.
[43] Metcalfe WK, Burke SM, Ahmed SS, Curran HJ. A hierarchical and comparative kinetic modeling study of C1–C2 hydrocarbon and oxygenated fuels. Int J Chem Kinet 2013;45(10):638–75.
[44] Burke SM, Metcalfe W, Herbinet O, Battin-Leclerc F, Haas FM, Santner J, et al. An experimental and modeling study of propene oxidation. Part 1: Speciation measurements in jet-stirred and flow reactors. Combust Flame 2014;161(11):2765–84.
[45] Ranzi E, Frassoldati A, Stagni A, Pelucchi M, Cuoci A, Faravelli T. Reduced kinetic schemes of complex reaction systems: fossil and biomass-derived transportation fuels. Int J Chem Kinet 2014;46(9):512–42.
[46] Pejpichestakul W, Ranzi E, Pelucchi M, Frassoldati A, Cuoci A, Parente A, et al. Examination of a soot model in premixed laminar flames at fuel-rich conditions. Proc Combust Inst 2019;37(1):1013–21.
[47] Pelucchi M, Cavallotti C, Cuoci A, Faravelli T, Frassoldati A, Ranzi E. Detailed kinetics of substituted phenolic species in pyrolysis bio-oils. React Chem Eng 2019;4(3):490–506.
[48] Rashidi MJ, Mehl M, Pitz WJ, Mohamed S, Sarathy SM. Cyclopentane combustion chemistry. Part I: Mechanism development and computational kinetics. Combust Flame 2017;183:358–71.
[49] Saggese C, Ferrario S, Camacho J, Cuoci A, Frassoldati A, Ranzi E, et al. Kinetic modeling of particle size distribution of soot in a premixed burner-stabilized stagnation ethylene flame. Combust Flame 2015;162(9):3356–69.
[50] Sgro L, Barone A, Commodo M, D'Alessio A, De Filippo G, Lanzuolo P, et al. Proc. Measurement of nanoparticles of organic carbon in non-sooting flame conditions. Proc Combust Inst 2009;32:689–96.
[51] Bladh H, Olofsson E, Mouton T, Simonsson J, Mercier X, Faccinetto A, et al. Probing the smallest soot particles in low-sooting premixed flames using laser-induced incandescence. Proc Combust Inst 2015;35:1843–50.
[52] Zhao B, Uchikawa H, Wang H. A comparative study of nanoparticles in premixed flames by scanning mobility particle sizer, small angle neutron scattering, and transmission electron microscopy. Proc Combust Inst 2007;31:851–60.
[53] Schenk M, Lieb S, Vieker H, Beyher A, Gölzhäuser A, Wang H, et al. Morphology of nascent soot in ethylene flames. Proc Combust Inst 2015;35:1879–86.
[54] Maricq MM. Coagulation dynamics of fractal-like soot aggregates. J Aerosol Sci 2007;38:141–56.
[55] Mueller CJ, Martin GC. Effects of oxygenated compounds on combustion and soot evolution in a DI diesel engine: broadband natural luminosity imaging. SAE Trans 2002;Jan 1:518–37.
[56] Marchese AJ, Dryer FL. The effect of non-luminous thermal radiation in microgravity droplet combustion. Combust Sci Technol 1997;124:371–402.
[57] Jackson GS, Avedisian CT. Modeling spherically symmetric droplet flames using complex chemistry: effects of droplet size and water addition on n-heptane droplet combustion. Combust Sci Technol 1996;115:127–47.
[58] Avedisian CT, Skyllingstad K, Cavicchi RC, Lippe C, Carrier MJ. Initiation of flash boiling of multicomponent miscible mixtures with application to transportation fuels and their surrogates. Energy Fuels 2018;32:9971–81.
[59] Avedisian CT. The Homogeneous nucleation limits of liquids. J Phys Chem Ref Data 1985;14(3):695–720.
[60] Dobbins RA. Soot inception temperature and the carbonization rate of precursor particles. Combust Flame 2002;130(3):204–14.